CONTENTS

1. Theoretical Mechanisms of Photogenerated Carrier Regulation

We have developed a transient carrier-concentration model, the core of which is a framework comprising five partial differential equations. These equations describe the temporal evolution of electrons, holes, and the acceptor, donor, and neutral states of vanadium ($N_{VA}(-)$, $N_{VD}(+)$, and $N_{VN}(0)$), and are numerically solved using MATLAB. **Fig. S1(a)** illustrates the electron transition processes occurring within the amphoteric impurity vanadium (V).

Carrier generation and recombination rates are denoted by G and R, respectively. G_{Dn} and G_{An} represent the rates of electron generation from the excitation of $N_{VD}(+)$ and $N_{VA}(-)$, respectively, while G_{DP} and G_{AP} denote the rates of hole generation from the excitation of $N_{VD}(+)$ and $N_{VA}(-)$. The processes R_{Dn}, R_{An}, R_{DP}, and R_{AP} represent the respective carrier capture events.

Fig. S1(b) presents the solution flowchart. Initially, the impurity ionization concentrations under dark steady-state conditions are computed using the charge neutrality equation.

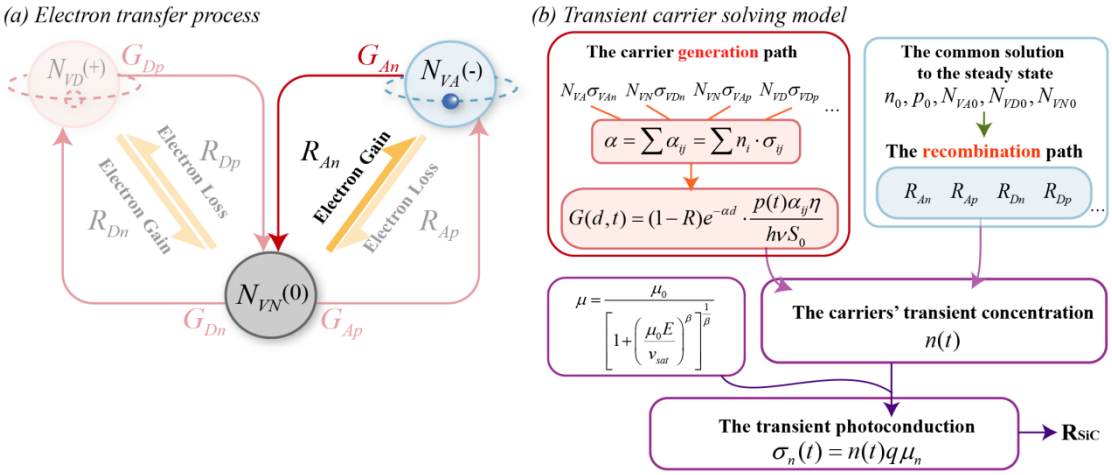

Fig. S1. (a) Electron transfer process. (b) Framework for solving transient carrier concentration.

The transient carrier-concentration framework is formulated as a set of partial differential equations:

$$\begin{aligned}
\frac{d\Delta n}{dt} &= G_{Dn} + G_{An} - R_{Dn} - R_{An} \\
\frac{d\Delta p}{dt} &= G_{Dp} + G_{Ap} - R_{Dp} - R_{Ap} \\
\frac{d\Delta V_A}{dt} &= G_{Ap} - G_{An} + R_{An} - R_{Ap} \\
\frac{d\Delta V_D}{dt} &= G_{Dn} - G_{Dp} + R_{Dp} - R_{Dn} \\
\frac{d\Delta V_N}{dt} &= G_{Dp} - G_{Dn} + G_{An} - G_{Ap} - R_{An} + R_{Ap} - R_{Dp} + R_{Dn}
\end{aligned} \tag{1}$$

Within this framework, the carrier generation term G can be expressed as:

$$G(d,t) = (1-R)e^{-\alpha d} \cdot \frac{p(t)\alpha_{ij}\eta}{h\nu S_0} \tag{2}$$

$$\alpha = \sum \alpha_{ij} = \sum n_i \cdot \sigma_{ij} = N_{VA}\sigma_{VAn} + N_{VN}\sigma_{VDn} + N_{VN}\sigma_{VAp} + N_{VD}\sigma_{VDp} \tag{3}$$

$$\sigma_{ij}(h\nu) = \frac{1}{n_r} \frac{8\pi e^2 h \left(E_{ij}\right)^{\frac{1}{2}} \left(h\nu - E_{ij}\right)^{\frac{3}{2}}}{3m^* c \left(h\nu\right)^3} \tag{4}$$

Here, R is the material surface reflectivity, d represents the depth of light penetration from the surface, α is the total optical absorption coefficient, which is the sum of the absorption coefficients of all optical channels (α_{ij}), $p(t)$ is the incident light power, η denotes the internal quantum efficiency (the ratio of electron generation to absorbed photons in the material), $h\nu$ is the photon energy, and S_0 is the illuminated area, which also corresponds to the electrode area. The ionization energy of the impurity level is denoted as E_{ij}.

Assuming the net electron capture rate at energy level E_t is the difference between the capture rate and the emission rate of electrons, the net capture rate of electrons is:

$$R_n = R_{cn} - R_{en} = C_n N^p n - E_n N^e = C_n [N^p n - N^e n'] \tag{5}$$

$$C_n = \sigma_t^n \nu_{th}^n, \quad C_p = \sigma_t^p \nu_{th}^p \tag{6}$$

Where C_n and E_n are the capture and emission cross-section constants, respectively. N^e and N^p represent the electron and hole concentrations at energy level E_t. The capture cross-section for electrons and the thermal velocity of electrons at this energy

level are denoted as σ_t^n and v_{th}^n, respectively. Without considering the degenerate factor, n' and p' are given by the following expressions:

$$n' = N_c \exp\left[-\frac{(E_c - E_t)}{kT}\right], \quad p' = N_v \exp\left[-\frac{(E_t - E_v)}{kT}\right] \tag{7}$$

Specifically, the net electron and hole capture rates at the V acceptor level are:

$$R_{An} = R_{Acn} - R_{Aen} = \sigma_{An} v_n (N_{VN} \cdot n - N_{VA} \cdot n'_A) \tag{8}$$

$$R_{Ap} = R_{Acp} - R_{Aep} = \sigma_{Ap} v_p (N_{VA} \cdot p - N_{VN} \cdot p'_A) \tag{9}$$

$$n'_A = g_A N_c \exp[-\frac{(E_c - E_{VA})}{kT}] \tag{10}$$

$$p'_A = (1/g_A) N_v \exp\left[-\frac{(E_{VA} - E_v)}{kT}\right] \tag{11}$$

The net electron and hole capture rates at the V donor level are:

$$R_{Dn} = R_{Dcn} - R_{Den} = \sigma_{Dn} v_n (N_{VD} \cdot n - N_{VN} \cdot n'_D) \tag{12}$$

$$R_{Dp} = R_{Dcp} - R_{Dep} = \sigma_{Dp} v_p (N_{VN} \cdot p - N_{VD} \cdot p'_D) \tag{13}$$

$$n'_D = (1/g_D) N_c \exp[-\frac{(E_c - E_{VD})}{kT}] \tag{14}$$

$$p'_D = g_D N_v \exp\left[-\frac{(E_{VD} - E_v)}{kT}\right] \tag{15}$$

If only the V acceptor level exists, the electron and hole lifetimes are:

$$\tau_n = n / R_{An} = \frac{1}{\sigma_{An} v_n (N_{VN} - N_{VA} \cdot n'/n)} \tag{16}$$

$$\tau_p = p / R_{Ap} = \frac{1}{\sigma_{Ap} v_p (N_{VA} - N_{VN} \cdot p'/p)} \tag{17}$$

If both V acceptor and V donor levels exist simultaneously, the electron and hole lifetimes are:

$$\tau_n = 1/(R_{An}/n + R_{Dn}/n) \tag{18}$$

$$\tau_p = 1/(R_{Ap}/p + R_{Dp}/p) \tag{19}$$

After solving the transient carrier concentration $n(t)$, the real-time voltage across the SiC device is extracted from the circuit model. From this, the mobility can be calculated. The high-field mobility is expressed as:

$$\mu_n = \frac{\mu_{n0}}{\left[1+\left(\frac{\mu_{n0}E}{v_{sat}}\right)^{\beta}\right]^{\frac{1}{\beta}}} \quad (20)$$

Finally, the electrical conductivity of the SiC material, dominated by the electron concentration, is derived using:

$$\sigma_n(t) = n(t)q\mu_n \quad (21)$$

The values of the parameters used in the theoretical model are shown in **Table S1.**

Table S1 Parameters for the Transient Carrier Model

Parameter	Value	Units
$\sigma_{VAn}/\sigma_{VDn}/\sigma_{VAp}/\sigma_{VDp}$ (1064 nm)	1×10^{-17} /0/0/0	cm^2
$\sigma_{VAn}/\sigma_{VDn}/\sigma_{VAp}/\sigma_{VDp}$ (532 nm)	$2.86\times10^{-17}/1.3\times10^{-17}/5.2\times10^{-19}/1.47\times10^{-17}$	cm^2
S_0	0.0962	cm^2
d	0.15	cm
R	0.1975	-
η	1	-
v_{th}^n/v_{th}^p	$1.33\times10^7/1.17\times10^7$	cms^{-1}
$\sigma_{An}/\sigma_{Ap}/\sigma_{Dn}/\sigma_{Dp}$	$1.5\times10^{-14}/1.5\times10^{-14}/2\times10^{-16}/2\times10^{-16}$	cm^2
g_A/g_D	4/2	-
μ_{n0}	225	$cm^2V^{-1}s^{-1}$
β	1.7	-
v_{sat}	2.2×10^7	cms^{-1}

Fig. S2(a) demonstrates the material's transient response to an incident light waveform with steep rise and fall edges. As the doping ratio increases, the relaxation times of both edges significantly increase. **Fig. S2(b)** shows that electron lifetime increases from 62 ps to 220 ps as the doping ratio rises, and its fluctuation with respect to light intensity amplitude also becomes more pronounced. **Fig. S2(c)** illustrates changes in modulation depth for different doping ratios under constant illumination. When the doping ratio is reduced from 0.8 to 0.4, the modulation depth improves from 60.5% to 95%. Although a higher doping ratio results in a higher peak electron concentration, the effective modulation of output voltage is stronger at lower ratios, as shown in **Fig. S2(d).** The material with a doping ratio of 0.4 yields a significantly higher

effective output voltage than that with a doping ratio of 0.8.

Fig. S2(e) and **Fig. S2(f)** show the output waveforms and frequency responses of devices with different carrier lifetimes triggered by lasers at various frequencies.

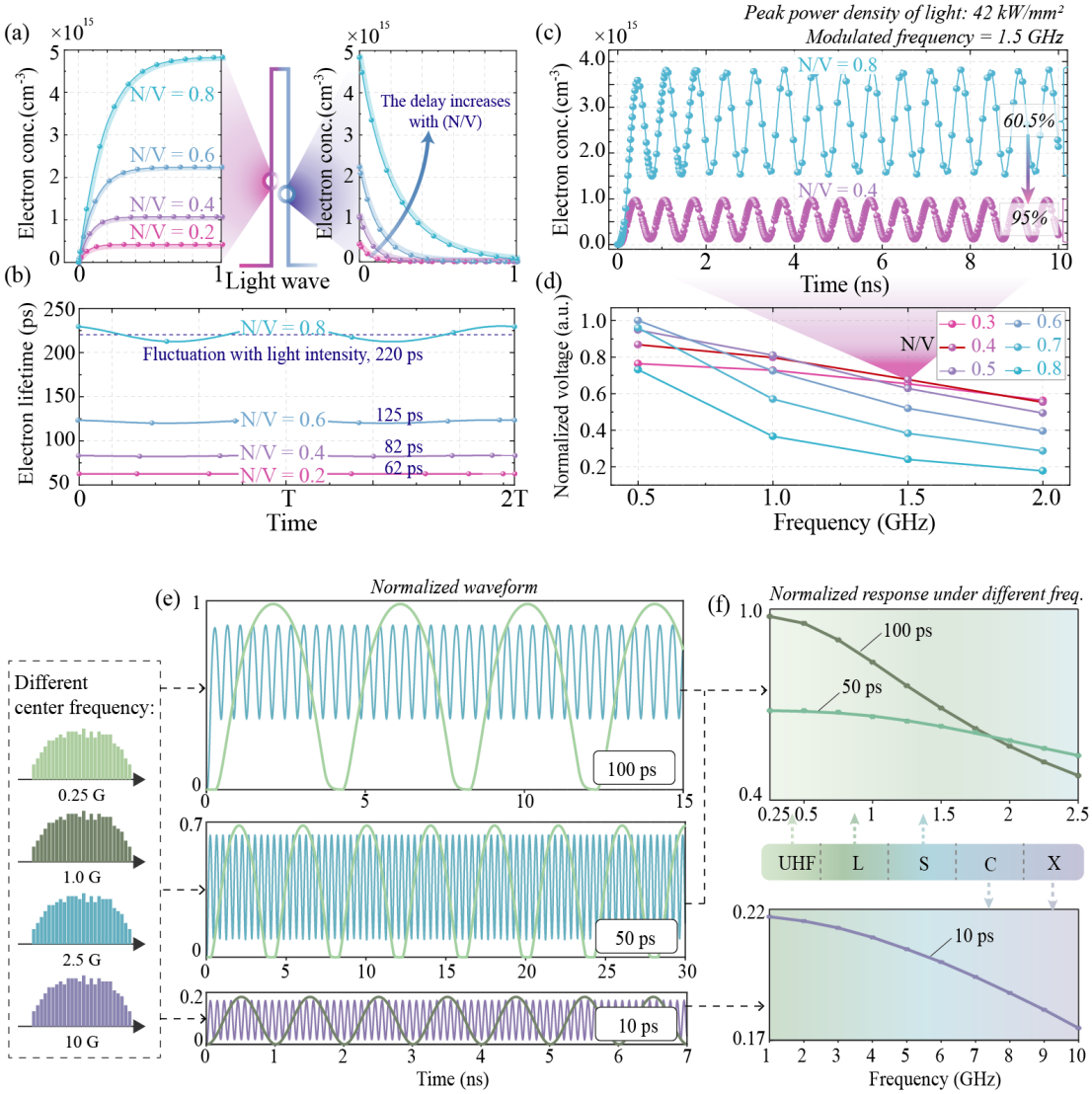

Fig. S2. (a) Effect of doping ratio on step-like optical signal response. (b) Effect of doping ratio on carrier lifetime. (c) Time-domain carrier concentration curves for doping ratios of 0.4 and 0.8. (d) Effect of doping ratio on the peak-to-peak output voltage. (e) and (f) Output waveforms and frequency response curves for carrier lifetimes between 10 to 100 ps.

The carrier capture processes are illustrated in **Fig. S3**. Due to the much smaller electron and hole capture cross-sections at the V donor level—by two orders of magnitude compared to the V acceptor level), we consider the V donor level to act as a slow recombination channel. Additionally, we compared simulation results under non-

intrinsic light excitation at 532 nm. In this case, valence-band electrons are also excited to the V acceptor level, leading to sustained occupation and reduced capture rate. Even at a doping ratio of 0.1, the electron lifetime exceeds 154 ps. As the doping ratio increases, hole lifetime exceeds electron lifetime, further reducing modulation depth and limiting effective output voltage. Therefore, we identify the V acceptor level as a medium-speed recombination channel under 532 nm excitation, and as a fast channel under 1064 nm excitation.

In summary, excitation using 1064 nm light in a material with an N/V doping ratio of 0.4 yields the most favorable transient-carrier response for broadband device applications.

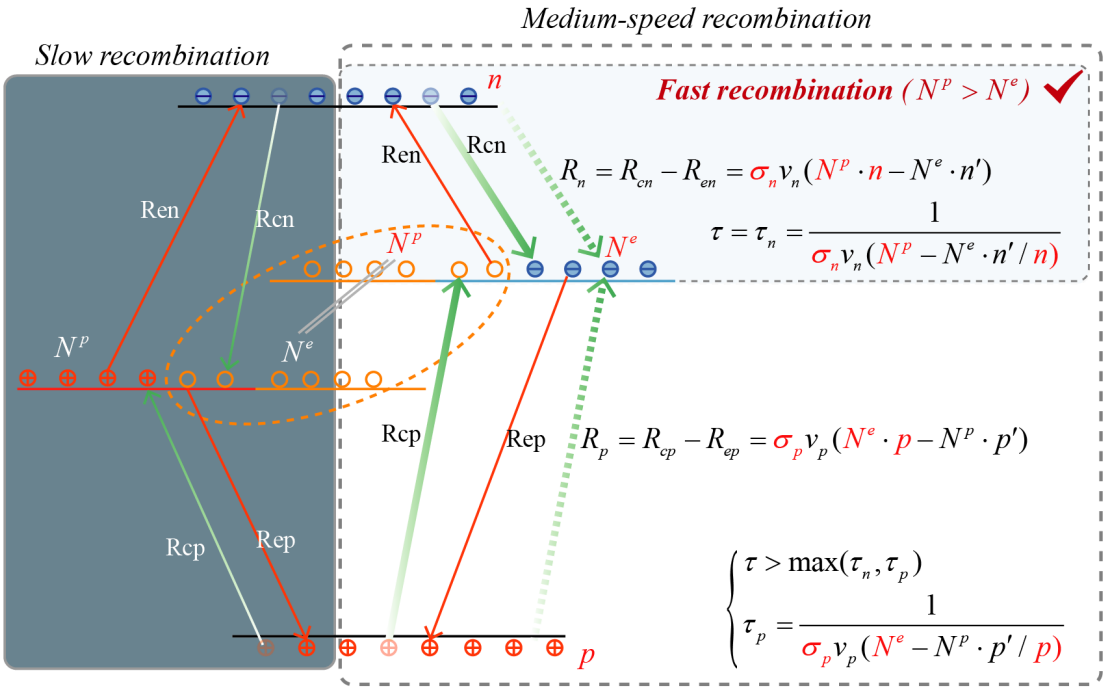

Note: N^e and N^p are the electron concentration and hole concentration at this energy level, respectively.
σ_n and σ_p are the electron capture cross-section and hole capture cross-section, respectively.
R_n and R_p are the net capture rates of electrons and holes, respectively.
R_{cn} and R_{cp} are the capture rates of electrons and holes, respectively.
R_{en} and R_{ep} are the emission rates of electrons and holes, respectively.

Fig. S3. Schematic diagram of the carrier capture process.

2. The Architecture of the High Peak Power Laser Source

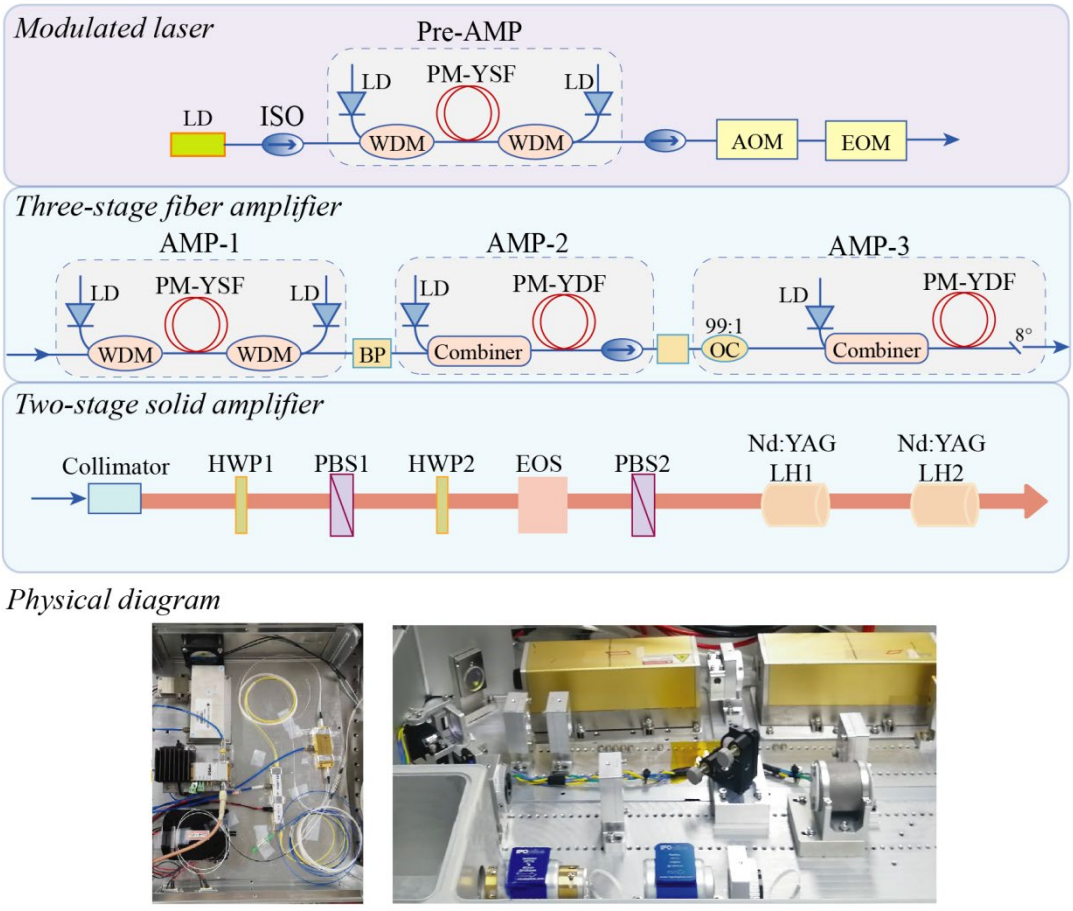

Fig. S4. High peak power laser source architecture: optical modulation section, fiber laser amplification section, solid-state laser amplification section, and physical diagram of the laser source [ref S1].

The time-domain multi-parameter tunable pulse-cluster seed laser comprises a pulse laser source (laser diode, LD), a single-stage fiber-core preamplifier (Pre-AMP), an acousto-optic modulator (AOM), and an electro-optic modulator (EOM). The circuit drives the narrowband semiconductor LD to generate pulses with adjustable pulse width and repetition frequency. After amplification by the preamplifier, the seed laser passes through the AOM, which filters out amplified spontaneous emission (ASE) and modulates the envelope of the pulse cluster via intensity modulation. Final shaping of the pulse cluster is accomplished by the EOM through additional intensity modulation.

To increase the peak power and pulse energy of the fiber amplifier output, a three-

stage fully polarized fiber amplifier system is employed for power amplification of the pulse-cluster laser. The first-stage amplifier adopts a bidirectional core-pumping configuration. It utilizes a single-mode, polarization-maintaining gain fiber with a core/cladding diameter of 6/125 μm, an absorption coefficient of ~250 dB/m at 975 nm, and a length of 2 m. The second-stage amplifier uses a forward cladding-pumping structure with a double-clad, polarization-maintaining ytterbium-doped fiber of 10/125 μm (core/cladding), an absorption coefficient of 4.8 dB/m at 975 nm, and a length of 4.5 m. Due to the relatively low repetition rate of the pulse cluster, ASE is generated in both the first and second stages. To suppress ASE, a 2 nm narrowband optical filter is placed at the output of each of the first two amplification stages.

The main amplifier employs a large-mode-area, highly-doped gain fiber (25/250 μm) with forward pumping, forming a high-power pulse-cluster laser amplification system. Ultimately, a peak power of 10 kW is achieved, with a 3 dB spectral width of 0.18 nm at maximum output power. Further power scaling is limited by stimulated Brillouin scattering (SBS) nonlinear effects.

At the output of the main amplifier's gain fiber, a polarization-maintaining fiber isolator is spliced to block back-reflected light from the downstream solid-state amplifier, thus protecting the fiber amplifier. An SMA-type fiber collimator with tail fiber is then spliced, directing the fiber output into the solid-state amplifier. The collimated beam has a spot diameter of ~1.36 mm. The solid-state amplifier mainly comprises an electro-optic switch and two Nd:YAG solid-state gain stages. The fiber laser beam first passes through a half-wave plate (HWP1) and a polarization beam splitter (PBS1), which further purify the polarization of the fiber-delivered pulse cluster.

To meet the repetition rate requirements of the OEMS-based tunable microwave generation system, a Pockels cell assembly—comprising HWP2, the electro-optic switch, and PBS2—is used to reduce the pulse cluster repetition rate from 25 kHz to 100 Hz, synchronized by a timing signal. The laser beam is then directed into the Nd:YAG gain media.

In the experimental setup, an 808 nm LD side-pumps the Nd:YAG crystal. To balance

beam quality and extraction efficiency, a crystal with a diameter of 3 mm, a doping concentration of 0.6%, and a length of 82 mm is used. Both ends are coated with anti-reflective coatings (99.9% transmission), and the output facet is angle-cut at 3° to suppress parasitic oscillation and backward feedback. Finally, the amplified pulse-cluster laser is output through the collimated optical path.

3. The Output Waveform of the Laser Source

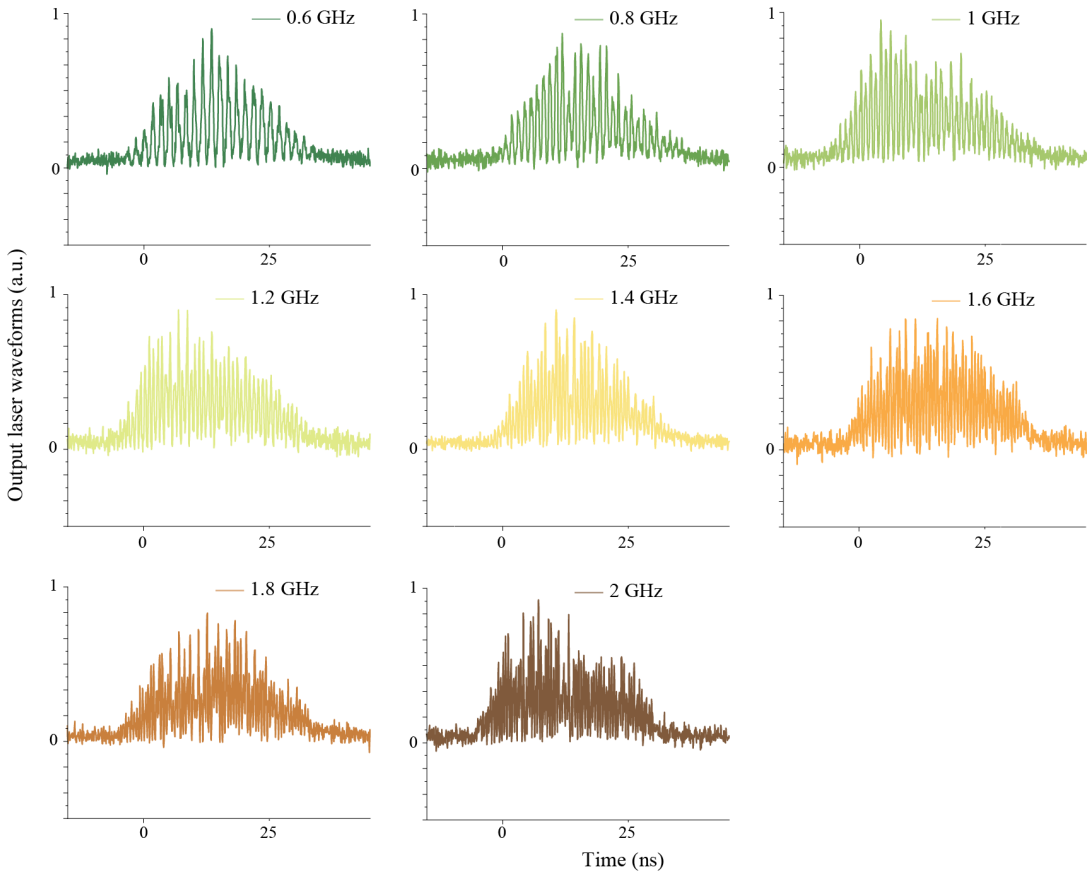

Fig. S5. Normalized waveform of the laser source output at a modulation frequency of 0.6-2 GHz with a single pulse energy of 30 mJ.

4. Output Waveform and Spectrum at Different Stages

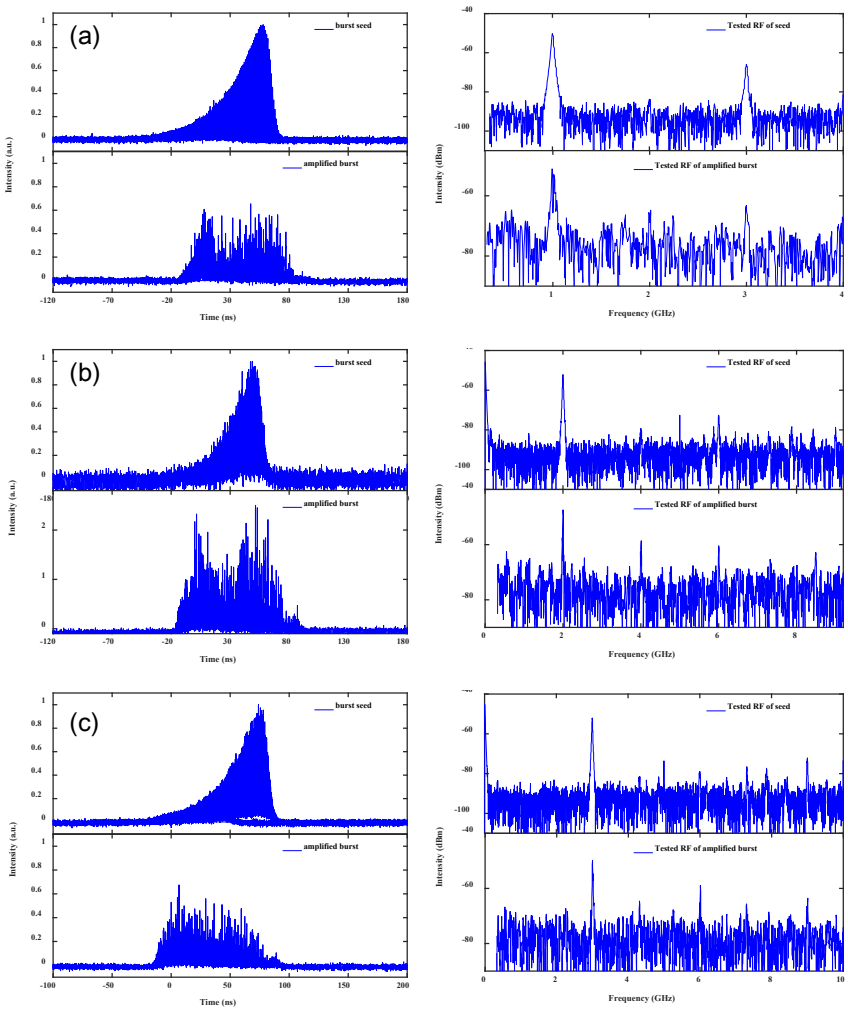

Fig. S6. Output waveform and normalized spectrum of the laser source at a modulation frequency of 1-3 GHz with a single pulse energy of 30 mJ.

The constructed pulse-cluster laser source emits at a wavelength of 1064 nm and delivers rectangular pulse clusters with a total energy of 30 mJ. The pulse cluster duration ranges from 30 ns to 100 ns, with each sub-pulse within the cluster exhibiting a 50% duty cycle. **Fig. S5** shows the normalized optical output waveform for a 30 ns pulse width and a single-pulse energy of 30 mJ. To enable more accurate spectral measurements, the pulse width was extended to 100 ns. The time-domain waveform and corresponding optical spectrum of the output are presented in **Fig. S6.**

5. Equivalent Circuit and RF Transmission Structure

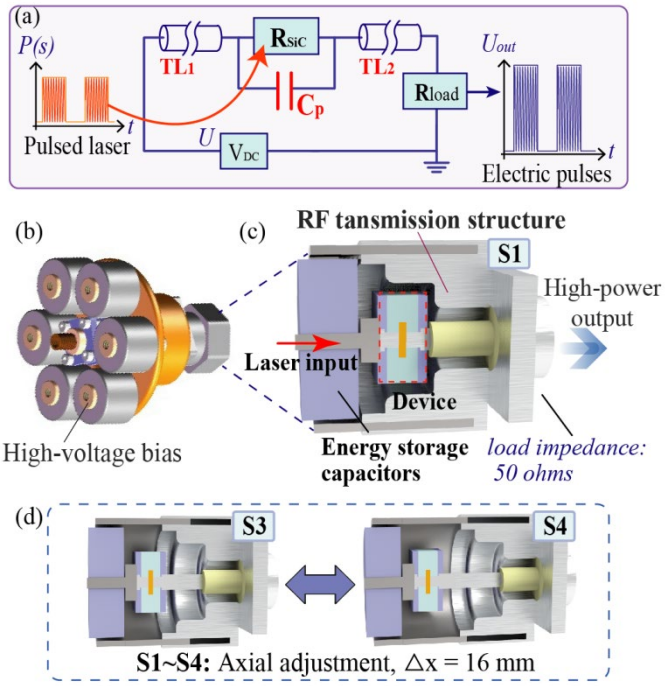

Fig. S7. (a) Equivalent circuit diagram of OEMS, (b) Physical diagram of RF transmission structure, (c) Schematic of the internal cross-section of the RF transmission structure, (d) Schematic cross-section of RF transmission structures with different dimensions.

Fig. S7(a) illustrates the circuit diagram of the optoelectronic microwave source (OEMS) based on photoconductive semiconductors. The circuit comprises a high-voltage power supply, energy storage capacitors (**Fig. S7(b)**), photoconductive semiconductor devices (PCSD), and radio-frequency (RF) transmission structures (**Fig. S7(c)**). These components collectively enable the generation of high-voltage electrical signals at the terminal electrodes of the semiconductor material, which are subsequently transmitted to a 50-ohm load. A high-peak-power laser is coupled into the semiconductor (R_{SiC}), thereby modulating its electrical conductivity at GHz frequencies.

6. Substrate Thickness and Load Resistance Design

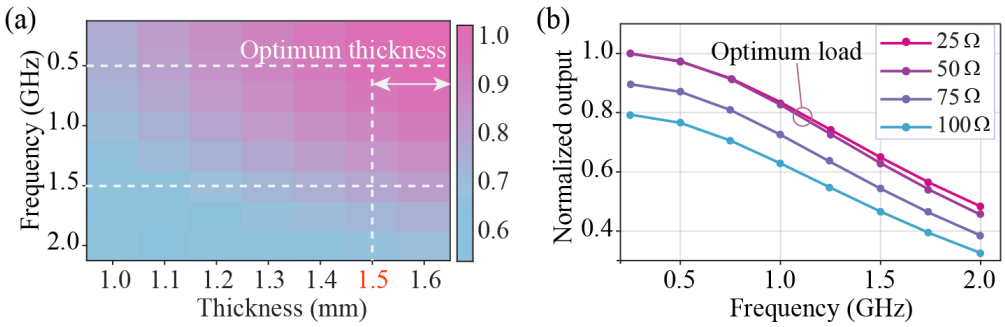

Fig. S8. The impact of substrate thickness and load resistance on circuit transmission characteristics.

Due to the approximate inverse relationship between substrate resistance and inter-stage capacitance ($C_p \approx \varepsilon S_0 / 4\pi kd$), and the near-proportional relationship between substrate resistance and breakdown voltage, a tradeoff must be achieved to determine the optimal substrate thickness that balances broadband performance and high-power output. Furthermore, the frequency response of the RF circuit is characterized by the square of the ratio of the circuit's output voltage to the DC bias voltage, which serves as a limiting factor for the system's overall bandwidth. By tuning the external coaxial transmission structure, the circuit's parasitic parameters (TL1, TL2) can be adjusted or suppressed to maximize output power within the desired frequency range—specifically the P–L band.

When the substrate thickness increases to 1.5 mm, the circuit's high-frequency response improves significantly, as illustrated in **Fig. S8(a). Fig. S8(b)** shows the trend in frequency response under various output load conditions. When the load resistance is within the range of 25–50 ohms, the power transmission efficiency reaches its peak.

7. Frequency Response Characteristics of Circuit with Different RF Transmission Structures

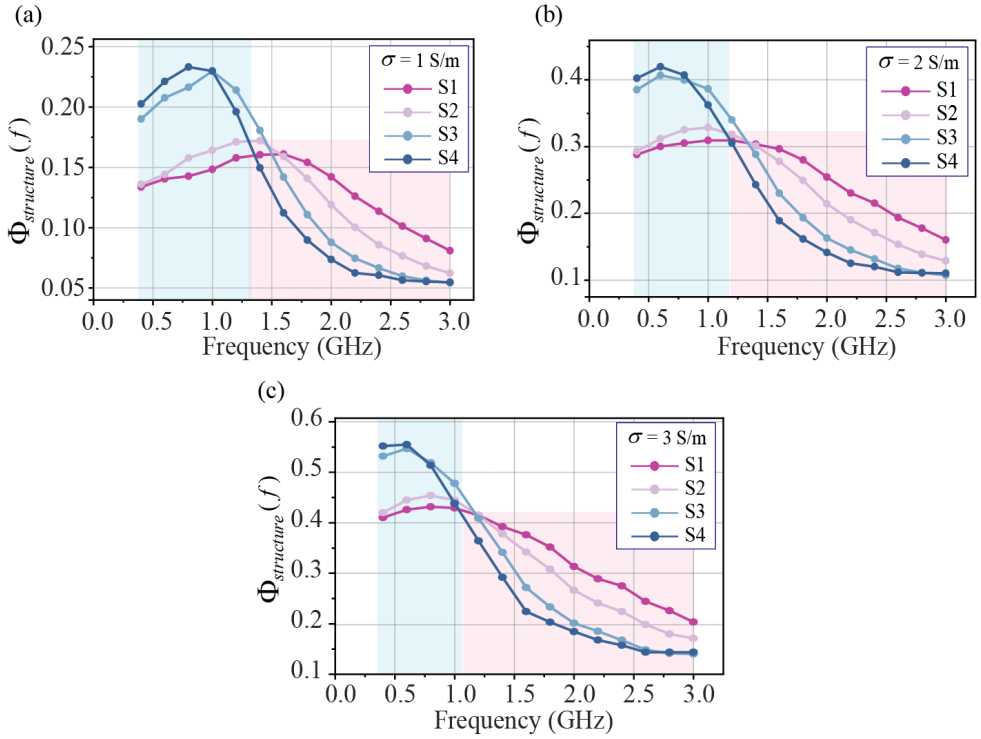

Fig. S9. Frequency response characteristics of the circuit with different RF transmission structures.

A tunable coaxial radio-frequency (RF) transmission structure was designed to match the output characteristics of the optoelectronic device, as shown in **Fig. S7(d)**. This structure enables the resonance gain point to shift from higher to lower frequencies by adjusting the axial length (S1-S4: Δx = 0 mm, 5.4 mm, 13.8 mm, 16.0 mm). The frequency response curves of the circuit ($\Phi_{structure}(f) = (V_{P-P} / V_{bias})^2$) under different optical intensities are presented in **Fig. S9(a)-(c)**. As shown in the frequency–power curve of the OEMS circuit, a 3-dB bandwidth of 0–3 GHz is achieved with a nearly flat frequency response across the range, even under varying incident light intensities.

8. High-Power Output Test Link of OEMS

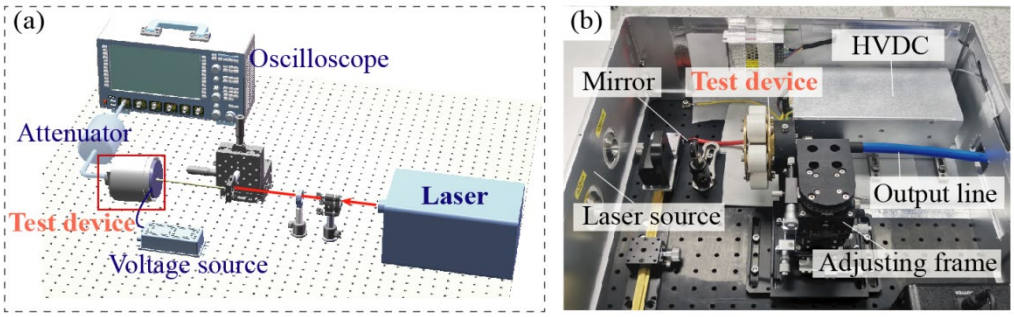

Fig. S10. Test link and actual test scene photo.

The experimental setup is shown in **Fig. S10 (a) and (b)**. The laser beam was coupled into the optical fiber via a focusing lens mounted on a three-dimensional adjustment bracket, and directed onto the photoconductive semiconductor. A high-voltage power supply charged the capacitors arranged around the device axis, effectively functioning as an energy source with a 22 kV output capacity. The 1064 nm laser used in the experiment operated at a repetition frequency of 100 Hz, with a pulse envelope width of 100 ns and an output energy of 30 mJ per pulse. The output microwave signal was transmitted through a 4 GHz/50 Ω attenuator to a sampling oscilloscope with a 4 GHz bandwidth. The definitions and measured values of the relevant physical quantities are provided in **Table S2.**

Table S2. The meanings and measured values of the physical quantities

Symbol	Meaning	Measured/calculated value	Unit
R_{load}	load resistance (port impedance)	50	Ω
k_1	attenuation factor of the attenuator	40.77	dB
k_2	attenuation factor of the directional coupler	1.57	dB
$k_1 \times k_2$	total attenuation factor	1.36×10^4	-
V_{test}	peak-to-peak voltage detected by the oscilloscope	1.21	mV
V_{P-P}	peak-to-peak voltage of the actual output signal	16.5	kV
P_{out}	output power	1.36	MW

9. High-Power Output Waveform and Spectrum

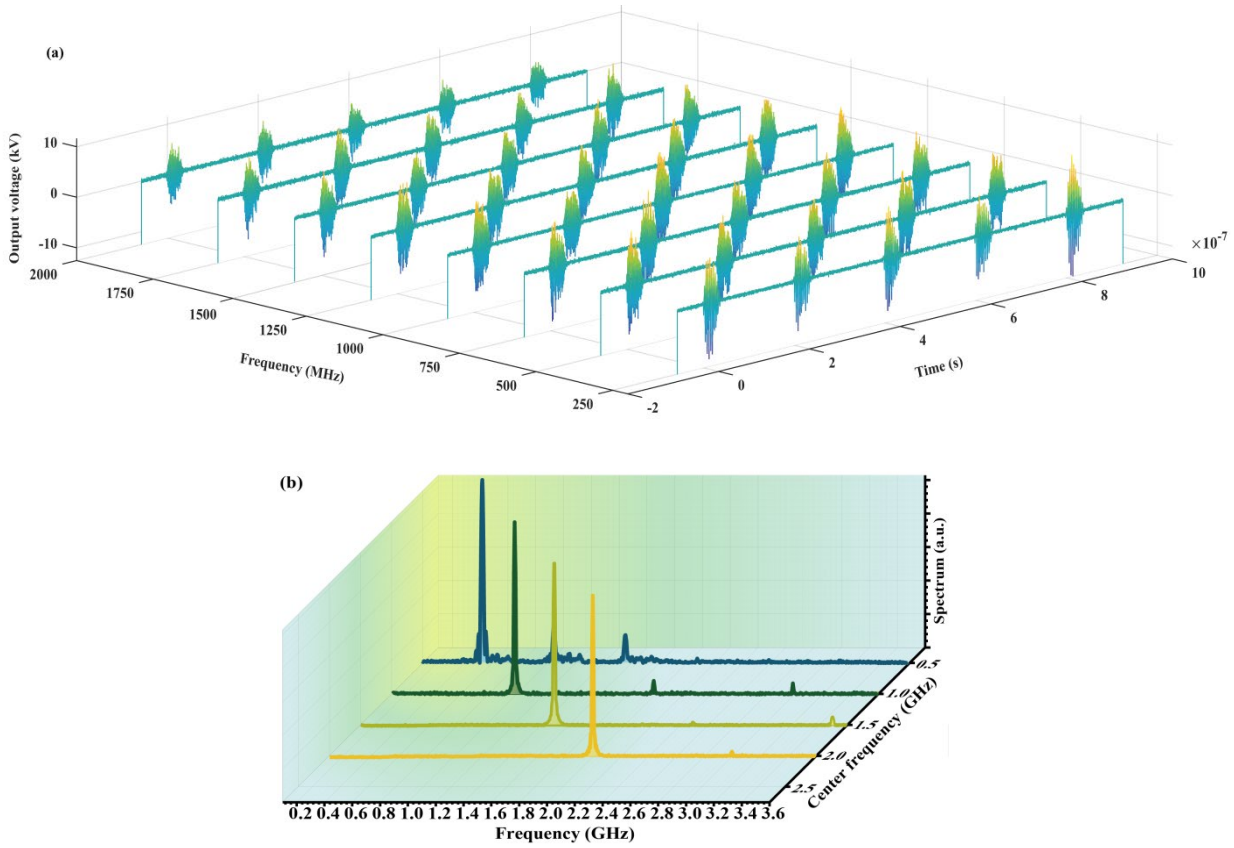

Fig. S11. (a) High-power output repetition frequency waveform of the optoelectronic microwave source within the 0.25-2 GHz frequency range. (b) Spectrum of the output microwave.

Because the test signal passes through both the coaxial-waveguide directional coupler and the broadband attenuator, it is necessary to calibrate these two measurement components prior to the experiment. This calibration is critical, as it significantly affects the accuracy and reliability of the experimental results. After calibration, the total attenuation factor of the test circuit ($k_1 \times k_2$) was obtained, and the actual output voltage was calculated using Equation (22). Subsequently, the output power delivered to the antenna or other load was derived from Equation (23).

$$V_{p-p} = V_{test} \times k_1 \times k_2 \qquad (22)$$

$$P_{out} = (V_{P-P} / 2)^2 / R_{load} \qquad (23)$$

As shown in **Fig. S11(a)**, when the output frequency ranged from 0.25 to 2 GHz, the

waveforms of the photocurrents closely matched those of the pulsed lasers. The corresponding output signals exhibited narrow spectral widths **(Fig. S11(b))**, indicating that vanadium-compensated semi-insulating silicon carbide (VCSI SiC) devices possess fast and linear response characteristics. Experimental results thus confirm that the SiC photoconductive system can generate frequency-tunable, megawatt-class microwave output signals, with continuous frequency adjustability from the P band to the L band. The response frequency can be further enhanced by optimizing the VCSI doping mechanism or reducing the device's interstage capacitance.

10. Carrier Lifetime Testing

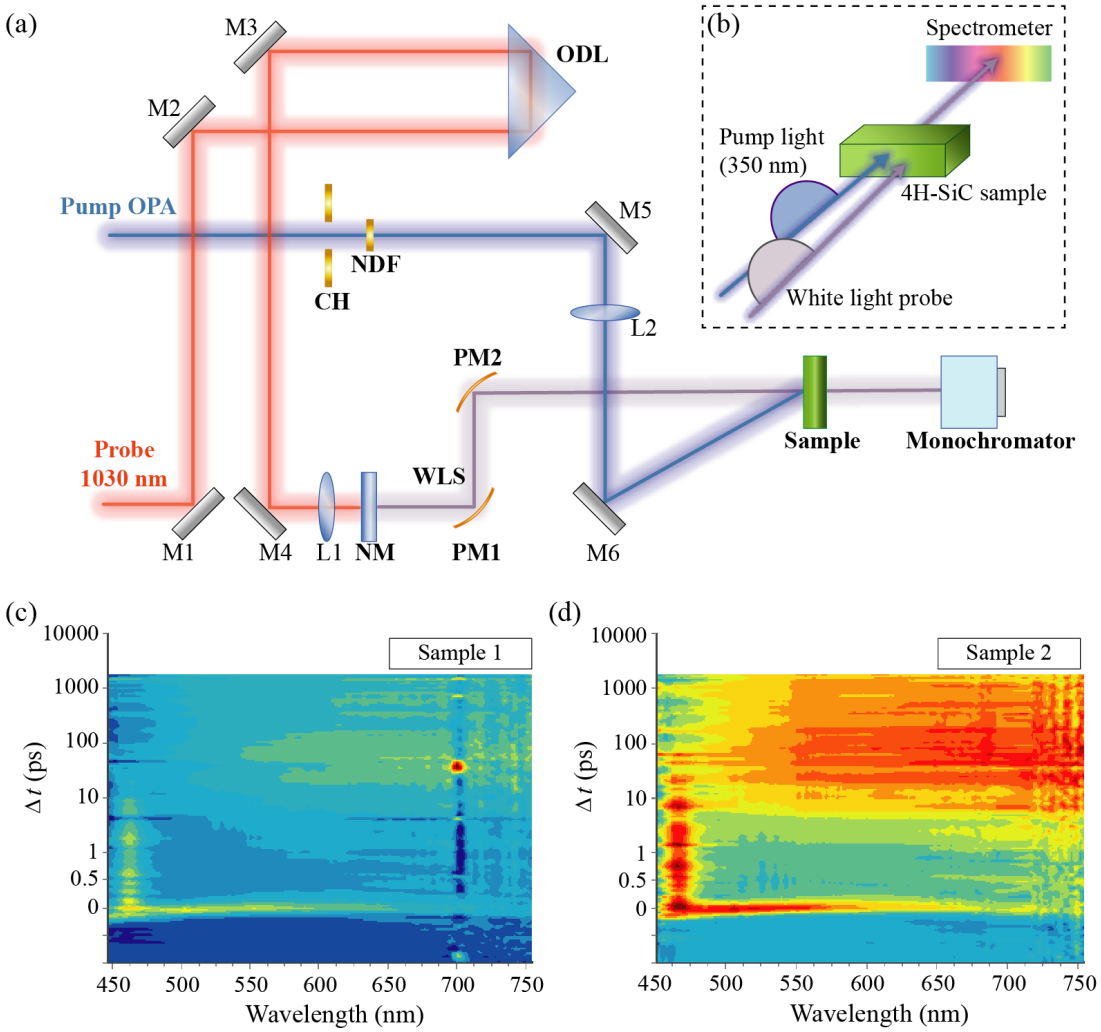

Fig. S12. (a) and (b) Carrier lifetime test link for materials. OPA: Optical parametric amplifier; M: Metal mirror; ODL: Optical delay line; L: Lens; CH: Chopper; NDF: Neutral density filter; NM: Nonlinear medium; WLS: White light supercontinuum; PM: Parabolic mirror; Sample: Sample; Monochromator: Grating monochromator. (b) Principle of transient absorption spectrum testing. (c) Transient absorption spectrum of Sample1. (d) Transient absorption spectrum of Sample2.

Carrier lifetime testing was performed on the designed substrate materials, referred to as Sample 1 and Sample 2. Using transient absorption spectroscopy, we investigated the ultrafast carrier dynamics and measured the transient absorption as a function of wavelength. The schematic diagram of the measurement optical path is shown in **Fig.**

S12(a) and **(b)**. The pump source used for bandgap excitation was an optical parametric amplifier (OPA, Light Conversion Orpheus, 190 fs, 6 kHz), modulated at 137 Hz by a chopper (CH) and focused onto the sample through a lens. A 1030 nm laser pulse was directed onto a nonlinear medium sapphire substrate (NM) to generate a white light supercontinuum (WLS) in the 450–780 nm range, which served as the probe light.

The transmitted signal through the sample was detected using a silicon diode array photodetector, and the delay between pump and probe pulses was recorded using an imaging spectrometer. By comparing the WLS intensity with and without pump excitation, we obtained the differential optical density (ΔOD) at various probe wavelengths (λ) and delay times (t), as defined in Equation (24).

$$\Delta OD(\lambda, t) = \lg \frac{I_{unpumped}}{I_{pumped}} \quad (24)$$

Here, $I_{unpumped}$ represents the white light supercontinuum intensity without pump excitation, and I_{pumped} is the intensity with pump excitation. Samples with doping ratios less than 1:10 (Sample 1) and approximately 1:2 (Sample 2) exhibited a transient absorption peak at 465 nm **(Fig. S12(c) and (d)).** The fitted carrier capture times at the vanadium (V) energy level were found to be 8.4 ps for Sample 1 and 80.2 ps for Sample 2.

11. Dark-State Breakdown Test of PCSD

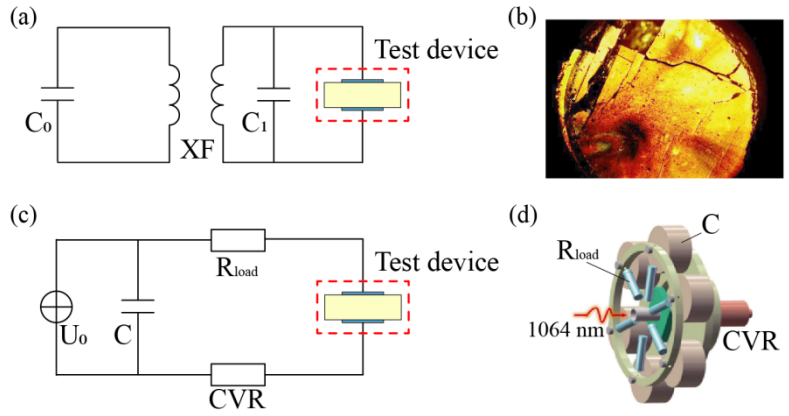

Fig. S13. (a) Dark-state breakdown test circuit, (b) Dark-state breakdown image, (c) Output current test circuit under illumination, (d) Device structure during output current test.

The dark-state high-voltage test circuit is shown in **Fig. S13(a)**. When the bias voltage reached 46 kV, the device experienced bulk breakdown. As illustrated in **Fig. S13(b)**, significant breakdown cracks appeared at the edges of the device, and both the transparent electrode and silver mirror electrode exhibited stress-induced deformation and cracking. While the theoretical breakdown electric field can reach 2–4 MV/cm, experimental breakdown occurred at the electrode edges at 46 kV, corresponding to an average breakdown electric field of 0.92 MV/cm. Simulation of the electrostatic field distribution inside the device revealed enhanced electric field concentration along the radial edge of the anode electrode, with a peak electric field reaching 1.6 MV/cm.

The output current test circuit under laser illumination and its corresponding device structure are shown in **Fig. S13(c)** and **(d)**. Under varying bias voltages and laser energy inputs, the temporal evolution of the average carrier concentration and the device resistance as functions of optical intensity are presented in **Fig. S14(a)** and **(b)**. Additionally, the peak current (I_{peak}), minimum on-resistance, and electric field were measured under 1–3 kV bias voltages and laser pulse energies ranging from 0.1 to 34 mJ. The peak current was used to calculate the minimum on-resistance and internal electric field, as defined by **Equation (25)**:

$$R_{SiC} = U_0 / I_{peak} - R_{load} (\sim 11.3\ \Omega) \qquad (25)$$

Where U_0 is the applied bias voltage, and R_{load} (11.3 Ω) represents the total resistance contributed by the load and circuit connections, including both lumped and distributed elements. The results are shown in **Fig. S14(c).** Under a laser energy of 34 mJ and a bias of 3 kV, the minimum R_{SiC} is approximately 5.3 Ω.

12. Conduction Current and Resistance Testing

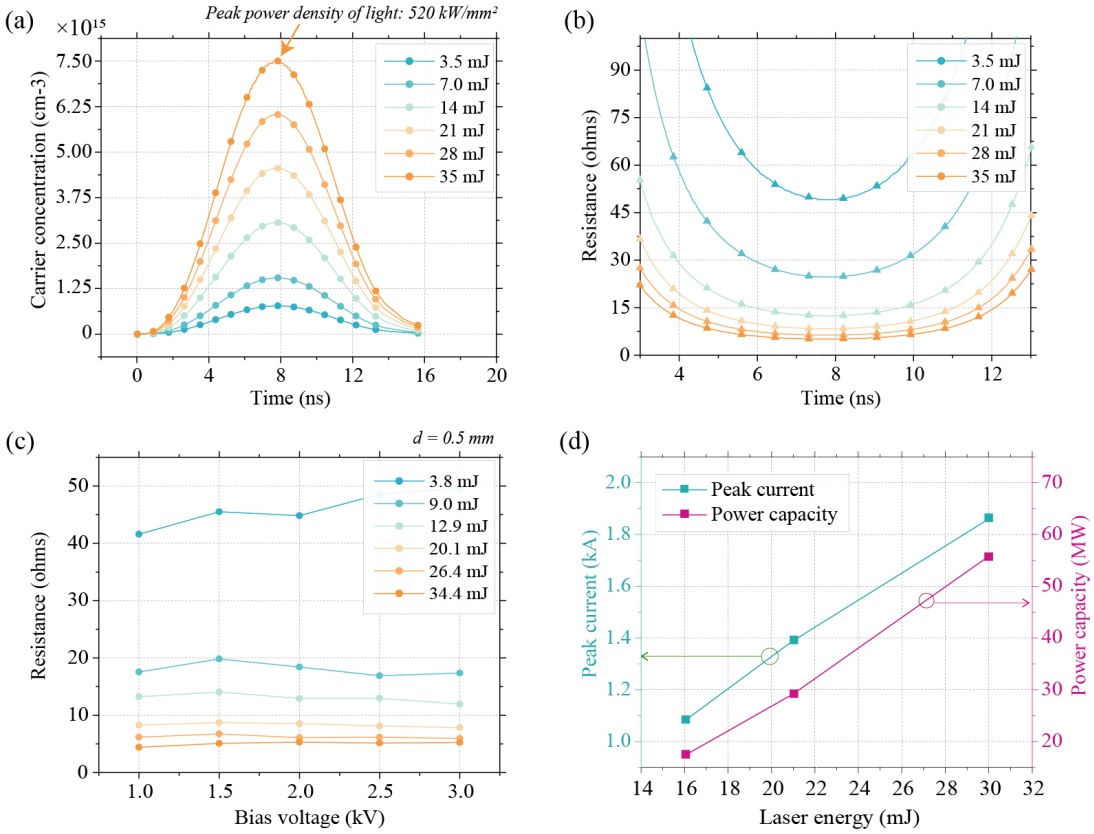

Fig. S14. (a) Temporal carrier concentration curve in the substrate with 1-35 mJ single-pulse light energy input, (b) Temporal resistance curve in the substrate with 1-35 mJ single-pulse light energy input, (c) Measured minimum on-resistance, (d) Measured current amplitude and power capacity.

We also tested the conduction current and power capacity under a 30 mJ laser input and bias voltages ranging from 16 kV to 30 kV. Power capacity is defined as the product of the bias voltage and conduction current. As shown in **Fig. S14(d)**, as the bias voltage increased from 16 kV to 30 kV, the peak current (I_{peak}) rose from 1.06 kA to 1.86 kA, while the power capacity increased from 17 MW to 55 MW.

13. Array Architecture and Test Environment

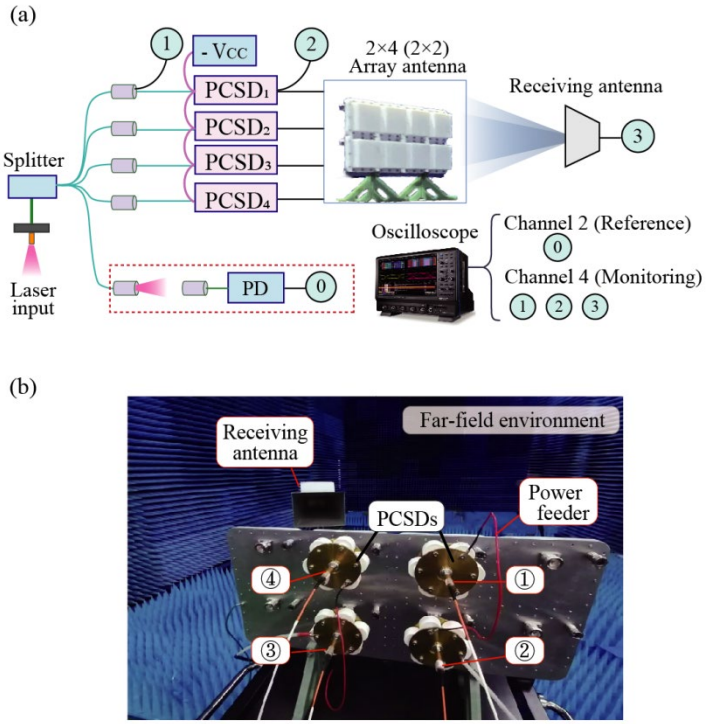

Fig. S15. (a) Array architecture, (b) Physical array and test environment.

14. OEMS Array Output Characteristics

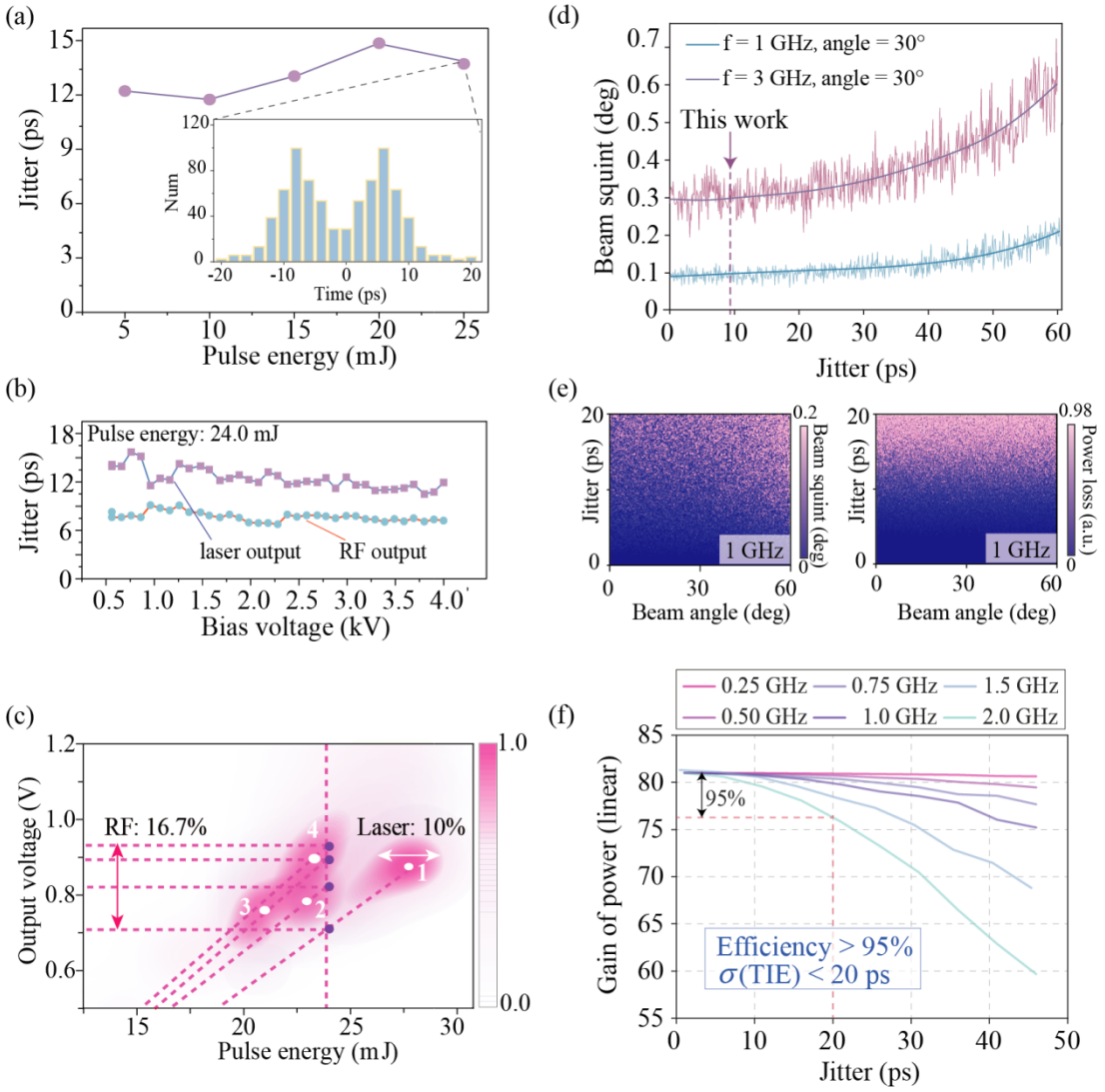

Fig. S16. (a) Time jitter of the OEMS output waveform as a function of single-pulse light energy, (b) Time jitter of the OEMS output waveform as a function of bias voltage under 24 mJ light intensity, (c) Amplitude consistency of the OEMS output waveform's photoconductive response, (d) Beam deflection angle of different frequency signals affected by time jitter, (e) Left: Beam pointing angle deviation influenced by scan angle and time jitter; right: Power synthesis loss influenced by scan angle and time jitter, (f) Synthesis efficiency of different frequency signals affected by time jitter.

Theoretically, with a properly set threshold, the measured time jitter reflects only phase jitter and is unaffected by amplitude jitter. Experimental results show that light intensity has minimal influence on output signal jitter. As illustrated in **Fig. S16(a)**,

when the light intensity increases from 5 mJ to 24 mJ, the average jitter of the optical signal increases slightly from 12 ps to 14 ps, consistently remaining below 15 ps. After significant accumulation, the jitter distribution of the signal approximates a bimodal profile, indicating the presence of both a random component and a spurious signal at a fixed frequency.

The overall time jitter of the OEMS output signal is shown in **Fig. S16(b)**. The results demonstrate that the bias voltage has negligible impact on the jitter of both optical and RF signals, which remain below 16 ps and 10 ps, respectively.

Cumulative measurements of the light signal's envelope amplitude are presented in **Fig. S16(c)**. The amplitude fluctuation caused by the laser delivery link is less than 10%. When the average incident optical energy is held constant, the RF output amplitude fluctuation is under 16.7%. Variability in substrate response can be effectively compensated by tuning the bias voltage.

For a 96-element true time delay (TTD) phased array, **Fig. S16(d)** shows that beam pointing deviation increases progressively with $\sigma(TIE)$ and radiation frequency. **Fig. S16(e)** displays the variations in pointing deviation and synthesis efficiency when the scanning range is 0° to 60° at 1 GHz. As seen in **Fig. S16(f)**, maintaining a $\sigma(TIE)$ below 20 ps allows the array to achieve over 95% synthesis efficiency across the 1–2 GHz frequency band.

15. Comparison of This Study with Other Microwave Source Metrics

Table S3. Summary of Solid-State Microwave Source Metrics

Ref.	Peak microwave power (W)	Frequency tuning range (GHz)	Types
30	2000	2.4-2.5	SSPA，Manufacturing Company: Fricke und Mallah Microwave Technology GmbH (Peine, Germany)
31	1200	0.902-0.928	SSPA，Model: SAIREM GLS 1200
32	150	1.15-1.23	GaN HEMT
33	230	1.55-1.6	GaN HEMT
34	40.7	0.6-0.9	Three-Stage Doherty Power Amplifier (GaN HEMT)
35	34	2.09-2.19	Three-Stage Doherty Power Amplifier (GaN HEMT)
36	40	1.8-2.1	Three-Stage Doherty Power Amplifier (GaN HEMT)
S2	1000	0.42-0.45	Paralleling two 500 W GaN HEMT
S3	700	0.5-0.6	GaN HEMT
S4	131	0.1-1	GaN HEMT

Table S4. Summary of Vacuum Electron Microwave Source Metrics

Ref.	Peak microwave power (W)	Center Frequency (GHz)	Frequency tuning range (GHz)	Types
38	0.1	1000	~100	Helix TWT
39	0.6	205	--	Staggered double-grating TWT
40	140	11.3	0.8	Helix TWT
S5	199.5	94.8	2.4	TWT
S6	100	230	20	Sheet Beam TWT
S7	20k	219	18	Gyrotron TWT
S8	310	220	35	Staggered double-grating TWT
42	5.06 k	13	10	Helix TWT

Table S5. Summary of Photoconductive Device Metrics

Ref.	Peak microwave power (W)	Frequency tunable	Rise Time(RT) / Pulse Width(PW)	Bandwidth (GHZ)	Mechanisms
48	14950	√	RT=520 ps	0.67	Bulk GaN PCSS(Linear)
49	10875	√	RT=412 ps	0.85	Bulk GaN PCSS(Linear)
50	210000	×	RT=300 ps	1.17	GaAs PCSS (Nonlinear)
51	11240	×	PW=1230 ps	0.81	GaAs PCSS(Nonlinear)
52	3380000	×	PW=11300 ps	0.088	GaAs PCSS(Nonlinear)
S9	50	√	--	10	Diode: Modified Single-Carrier Detector (MUTC),
S10	29.8	√	--	1.6	Si/SiGe Phototransistor
S11	720000	√	--	~ 0.7	SiC PCSS
This work		√	--	1.25	SiC PCSS

The abbreviation PCSS refers to Photoconductive Semiconductor Switch. For devices without inherent frequency tuning capabilities, the potential frequency response range is estimated using the formulas $BW = 0.35 / rise\ time$ and $BW = 0.35 / pulse\ width$. For unipolar output devices, the direct current (DC) component must be filtered out, and the microwave peak output power is calculated using the expression $P_{MW} = P_{out} / 4$.

Table S4. Summary of Voltage-Current Metrics for Photoconductive Devices

Ref.	Bias voltage (kV)	On current (A)	Material and Mechanism
S12	12	840	SiC PCSS
S13	16	1400	SiC PCSS
S14	18	591	SiC PCSS
S15	20	50	SiC PCSS
S16	20	100	SiC PCSS
S17	26	450	SiC PCSS
S18	32.2	938	SiC PCSS
S19	13	200	SiC PCSS
S20	11	104	SiC PCSS
S21	2.22	44	SiC PCSS
This work	30	18.6k	SiC PCSS

Reference

[1] H. Xuan, Z. Bin, L. Shuailin, Y. Linyong, Y. Jinmei, W. Qilin, Z. Yuxin, X. Tao, and H. Jing, “High-power linear-polarization burst-mode all-fibre laser and generation of frequency-adjustable microwave signal,” High Power Laser Science and Engineering, vol. 9, no. 13, pp. e13–e13, 2021.

[2] G. Formicone, J. Burger, and J. Custer, “A UHF 1-kW solid-state power amplifier for spaceborne SAR,” 2017 IEEE Topical Conference on RF/Microwave Power Amplifiers for Radio and Wireless Applications (PAWR), 2017.

[3] X. Ma, B. Duan, and Y. Yang, “A 500–600 Mhz GaN power amplifier with RC–LC stability network,” Journal of Semiconductors, p. 085003, 2017.

[4] A. Raza and J. Gengler, “Design of a 110 W wideband inverse class-F GaN HEMT power amplifier with 65% efficiency over 100-1000 MHz bandwidth,” 2019 IEEE Topical Conference on RF/Microwave Power Amplifiers for Radio and Wireless Applications (PAWR), 2019.

[5] T. Zhenfeng, Z. Jinling, and Y. Song, “Innovative W-band through-wall radar with sector scanning: Utilizing traveling wave tubes for enhanced penetration,” IEEE Sensors Journal, vol. 24, no. 19, p. 1, 2024.

[6] G. Shu, H. Pan, X. Xie, S. Ma, J. Tang, S. Liu, M. Li, C. Ruan, and W. He, “Study of magnetic focusing structures for 220 Ghz sheet beam traveling wave tubes,” IEEE Transactions on Terahertz Science and Technology, vol. 15, no. 1, pp. 120–127, 2025.

[7] Y. Cao, Y. Ma, G. Liu, Y. Wang, W. Jiang, Y. Yao, J. Wang, and Y. Luo, “Design and measurement of a mode-suppression circuit for a G-band gyrotron traveling wave tube,” IEEE Transactions on Terahertz Science and Technology, vol. 14, no. 1, pp. 91–97, 2024.

[8] W. Wang, Z. Zhang, P. Wang, Y. Zhao, F. Zhang, and C. Ruan, “Double-mode and double-beam staggered double-vane traveling-wave tube with high-power and broadband at terahertz band,” Scientific reports, vol. 21, no. 1, p. 12012.

[9] F. Quinlan, “The photodetection of ultrashort optical pulse trains for low noise microwave signal generation,” Laser Photonics Reviews, vol. 17, no. 12, 2023.

[10] V. Thary, C. Algani, P. Chevalier, and J.-L. Polleux, “Low-cost and low-voltage Si/SiGe phototransistor with high responsivity at 900 nm for microwave photonics applications,” IEEE Electron Device Letters, vol. 46, no. 2, pp. 239–242, 2025.

[11] N. S. D., H. S., and P. B. R, “Triaxial photoconductive switch module,” US Patent Application, US20170264291A1, September 14, 2017.

[12] C. Penghui, H. Wei, G. Hui, and Z. Yuming, “Performance of a vertical 4H-SiC photoconductive switch with AZO transparent conductive window and silver mirror reflector,” IEEE Transactions on Electron Devices, vol. 65, no. 5, pp. 2047–2051, 2018.
[13] S. J. Stephen, “Wide bandgap extrinsic photoconductive switches,” Ph.D. dissertation, University of California, Davis, CA, USA, 2013.
[14] W. Qilin, X. Tao, Z. Yuxin, Y. Hanwu, and H. Wei, “The test of a high-power, semi-insulating, linear-mode, vertical 6H-sic pcss,” IEEE Transactions on Electron Devices, vol. 66, no. 4, pp. 1837–1842, 2019.
[15] L. Wang, X. Chu, Q. Wu, T. Xun, H. Yang, J. He, and J. Zhang, “Effects of high-field velocity saturation on the performance of V-doped 6H silicon-carbide photoconductive switches,” IEEE Journal of Emerging and Selected Topics in Power Electronics, vol. 9, no. 4, pp. 4879–4886, 2021.
[16] B. Wang, L. Wang, X. Niu, X. Chu, M. Yi, J. Yao, and T. Xun, “Breakdown behavior of SiC photoconductive switch with transparent electrode,” AIP Advances, vol. 12, no. 8, p. 085210, 2022.
[17] M. Daniel, S. W. III, B. Alan, N. Andreas, and D. James, “High power lateral silicon carbide photoconductive semiconductor switches and investigation of degradation mechanisms,” IEEE Transactions on Plasma Science, vol. 43, no. 6, pp. 2021–2031, 2015.
[18] M. Daniel, W. Chris, T. David, N. Andreas, and D. James, “Overview of high voltage 4H-SiC photoconductive semiconductor switch efforts at texas tech university,” in 2014 IEEE International Power Modulator and High Voltage Conference (IPMHVC), 2014.
[19] Y. Li, L. Xiao, C. Luan, X. Sun, H. Sha, J. Jiao, B. Yang, D. Li, Y. Qin, X. Chen, H. Li, and X. Xu, “Ultrafast characteristics of integrated high-power photoconductive semiconductor switch based on 4H-SiC substrate,” IEEE Transactions on Electron Devices, vol. 72, no. 1, pp. 128–134, 2025.
[20] H. Jia, H. Long, M. Zhenzhen, Z. Li, Y. Yingxiang, Y. Xianghong, S. Yue, L. Xin, and L. Chunliang, “Study on photoelectric efficiency and failure mechanism of high purity 4H-SiC PCSS,” IEEE Transations on Electron Devices, vol. 70, no. 11, pp. 1–7, 2023.
[21] X. Sun, L. Xiao, C. Luan, Z. Feng, H. Sha, Y. Li, J. Jiao, Y. Qin, X. Chen, H. Li, and X. Xu, “Low on-resistance and high peak voltage transmission efficiency based on high-purity 4H-SiC photoconductive semiconductor switch,” IEEE Transactions on Power Electronics, vol. 39, no. 2, pp. 2013–2019, 2024.